The effect of Fe–Rh alloying on CO hydrogenation to C_{2+} oxygenates

Robert M. Palomino [a], Joseph W. Magee [a], Jordi Llorca [c], Sanjaya D. Senanayake [b], Michael G. White [a,b,⇑]

[a] Department of Chemistry, Stony Brook University, Stony Brook, NY 11974, United States
[b] Chemistry Department, Brookhaven National Laboratory, Upton, NY 11973, United States
[c] Institute of Energy Technologies and Centre for Research in NanoEngineering, Technical University of Catalonia, Diagonal 647, 08028 Barcelona, Spain

Keywords:
Ethanol synthesis
Bimetallic catalysts
CO hydrogenation

abstract

A combination of reactivity and structural studies using X-ray diffraction (XRD), pair distribution function (PDF), and transmission electron microscopy (TEM) was used to identify the active phases of Fe-modified Rh/TiO_2 catalysts for the synthesis of ethanol and other C_{2+} oxygenates from CO hydrogenation. XRD and TEM confirm the existence of Fe–Rh alloys for catalyst with 1–7 wt% Fe and """2 wt% Rh. Rietveld refinements show that FeRh alloy content increases with Fe loading up to """4 wt%, beyond which segregation to metallic Fe becomes favored over alloy formation. Catalysts that contain Fe metal after reduction exhibit some carburization as evidenced by the formation of small amounts of Fe_3C during CO hydrogenation. Analysis of the total Fe content of the catalysts also suggests the presence of FeO_x also increased under reaction conditions. Reactivity studies show that enhancement of ethanol selectivity with Fe loading is accompanied by a significant drop in CO conversion. Comparison of the XRD phase analyses with selectivity suggests that higher ethanol selectivity is correlated with the presence of Fe-Rh alloy phases. Overall, the interface between Fe and Rh serves to enhance the selectivity of ethanol, but suppresses the activity of the catalyst which is attributed to the blocking or modifying of Rh active sites.

1. Introduction

The need to develop alternative sources of liquid fuels has led to renewed interest in developing catalysts for the efficient conversion of synthesis or ''syn'' gas ($CO + H_2$), derived from biomass, coal, and natural gas, to simple alcohols and higher oxygenates [1–15]. Currently, the only industrially applied process involves syngas conversion to methanol over a Cu-based catalyst ($Cu–ZnO/Al_2O_3$) at temperatures above 500 K [1]. While Cu-based catalysts are effective for methanol synthesis, they have poor performance for the production of ethanol and other C_{2+} oxygenates, which is desirable for its higher energy density, ease of handling, and nontoxicity. The search for new catalysts for higher oxygenate synthesis has taken a number of different approaches including the chemical modification of Cu-based methanol catalysts (metal promoters and doping), modified Fischer–Tropsch catalysts (Co, Ru, and Fe), and promoted MoS_2-based catalysts [2,3].

Among the transition metals, Rh surfaces are known to promote C–C coupling, which should allow the direct conversion of syngas to ethanol and C_{2+} oxygenates, yet Rh-based catalysts primarily produce methane when used without promoters [2,3]. Various promoters (Fe, CeO_2, V, La, Mn, Ag, Ti, Ir) have been shown to increase ethanol selectivity, with Fe being particularly effective due to its combined methane suppression and the enhancement of ethanol production [2–6]. Studies have shown that Fe loading up to 10 wt% has increased ethanol production while suppressing methane formation for Fe-promoted Rh/Al_2O_3 [6]. Metal dopants such as Fe are thought to improve performance by increasing the barrier for methane formation and/or decreasing the barrier for CO insertion [7]. Selectivity studies performed by Haider et al., also show that both unpromoted and Fe-promoted Rh catalysts exhibit enhanced activity and selectivity for oxygenates when the support is changed from silica to titania [4]. The authors attribute this to an increase in the number of active sites, which would be caused by increased dispersion and/or an enhanced particle–support interface. By modifying Rh-promoter and Rh-support interactions, the activity and selectivity to alcohols can be enhanced at the expense of the least desirable product, hydrocarbons such as methane.

A recent X-ray absorption spectroscopy (XAS) study of titania-supported FeRh catalysts during CO hydrogenation was performed by Gogate and Davis [5]. Using XANES and EXAFS, they determined the principle phases to be metallic Rh and FeO when catalysts were reduced and under CO hydrogenation conditions. One important insight is that there was no change in the atomic and electronic structures when the reduced sample was exposed to syngas ($H_2 + CO$) at 543 K at 1 bar total pressure. The EXAFS data

⇑ Corresponding author at: Chemistry Department, Brookhaven National Laboratory, Upton, NY 11973, United States.
E-mail address: mgwhite@bnl.gov (M.G. White).

did not conclusively indicate Fe–Rh bonding, but did show Rh bonded to Ti or lattice-bound oxygen with bond lengths of 2.53 Å and 2.48 Å, respectively. This conclusion was supported by other studies that found evidence of either Rh–Ti bonding or Rh bonding to lattice-bound oxygen in the TiO_2 [8–10]. Subsequent transmission electron microscopy (TEM) studies suggest intimate contact of Rh and Fe through the simultaneous detection of Rh and Fe in the same particles studied using spot scans of energy-dispersive spectroscopy (EDS) [4]. The combined results of these studies suggest that direct contact of Rh with both Fe and Ti is likely to be responsible for the enhanced activity and selectivity of these bimetallic catalysts. This could be due to an ensemble effect where Fe blocks active sites for hydrogenation of CH_x or a ligand effect where an interaction occurs between Rh and Fe or TiO_2 that creates/increases active sites responsible for CO insertion.

In this work, we used an array of X-ray structural techniques and TEM imaging to determine the structure of FeRh bimetallic catalysts supported on titania. Bimetallic catalysts tested consisted of Rh (""2 wt%) supported on TiO_2 with various amounts of Fe (1–7 wt%). X-ray diffraction (XRD) was used to identify and quantify the amount of each phase in the catalysts (e.g., FeRh alloy, Fe carbides, and oxides), and pair distribution functions (PDF) provided information on local atomic structure (bond lengths and nearest neighbors) and changes in coordination between different Fe concentrations under reactive conditions. In general, these studies show that increasing Fe concentration results in the formation of Fe-rich alloys, but CO hydrogenation conditions induce a carburization and oxidation of metallic Fe in catalysts with Fe loadings >4 wt%. Reactivity studies using a plug-flow reactor and gas chromatography for product quantification were used to correlate catalyst composition with selectivity for ethanol and methane formation from CO hydrogenation. The selectivity for ethanol peaks (""55%) at an Fe loading of ""4.5 wt% and closely follows the Fe-Rh alloy content of the catalysts. The addition of Fe also suppresses methane formation and significantly lowers overall CO conversion.

2. Experimental methods

2.1. Sample preparation and characterization

The Fe–Rh/TiO_2 catalysts were prepared via incipient wetness impregnation by the dissolution of rhodium(III) nitrate hydrate ($Rh(NO_3)_3$-xH_2O) and iron(III) nitrate nonahydrate ($Fe(NO_3)_3$-$9H_2O$) in distilled deionized water. The resultant aqueous solution was then added dropwise to Degussa P-25 titanium dioxide powder (pretreated at 450 oC in air for 4 h) with kneading to form a paste which is then dried at 180 oC overnight and subsequently calcined at 450 oC in air for 4 h. The iron(III) nitrate nonahydrate was varied to produce iron weight percentages ranging from 1% to 8%, while rhodium(III) nitrate hydrate concentration was unchanged to produce ""2 wt% Rh in the catalysts. A catalyst containing 2 wt% Fe/TiO_2 was also synthesized to compare with Rh-containing catalysts. Calcined catalysts were ground to produce a fine powder. The atomic compositions of the as-prepared catalysts were determined by inductively coupled plasma-optical emission spectroscopy (ICP-OES) (Galbraith Laboratories). As shown in Table 1, the ICP-OES results indicate that Rh remains relatively constant at ""1.7 wt%, while the content Fe ranges from 1.0 to 7.3 wt%. The different Fe-Rh catalysts will hereon be denoted by the amount of Fe loading (1FeRh, 2FeRh, 3FeRh, 4FeRh, and 7FeRh).

TEM (Tecnai G^2 F20 S-TWIN) was used to determine the Fe-Rh particle dispersion and size distribution before and after reaction. Catalyst samples were drop-cast from alcohol suspensions onto holey carbon Cu grids. The point-to-point resolution was

Table 1
Results of ICP-OES elemental analysis of Rh and Fe loading (wt%) for different Fe-modified Rh/TiO_2 catalyst samples.

Sample name	Fe loading (wt%)	Rh loading (wt%)
Rh	0	1.9
Fe	1.9	0
1FeRh	1.0	1.7
2FeRh	2.2	1.7
3FeRh	3.4	1.7
4FeRh	4.5	1.7
7FeRh	7.3	1.6

0.24 nm, and the resolution between lines was 0.10 nm. Energy-dispersive spectroscopy (EDS) was used to determine rela- tive amounts of Rh and Fe, both overall and in selected particles. The characteristic X-rays generated from each element upon expo- sure to the electron beam were measured and used to qualitatively determine the ratio of Fe:Rh in each sample. High-resolution TEM (HRTEM) was utilized to determine size distributions and crystallographic domains of selected particles.

2.2. Reactivity studies

Reactivity studies were carried out to determine selectivity toward various molecular products during CO hydrogenation. The catalyst was loaded into a 1/8^{00} OD quartz capillary tube plugged with quartz wool. Sample heating is provided by a filament wrapped around the capillary [16]. The temperature was monitored with a thermocouple in close contact with the sample. Sample temperature was controlled via current with a power supply connected to the filament heater. Reactant gases (CO/H_2) flowing through the reactor were controlled by mass flow controllers (MKS Instruments), and the output of the reactor was directed into the gas chromatograph (Agilent 3000A Micro GC) via a heated 1/8^{00} OD stainless steel tube. The GC is equipped with 3 different columns for separating methane and carbon monoxide (molecular sieve MS-5A), higher hydrocarbons (Agilent Plot-U), and oxygenates (Stabilwax). All columns use a thermal conductivity detector (TCD) for the quantification of the products separated in the columns. The GC was calibrated for the main products observed from CO hydrogenation under reaction conditions (methane, ethane, ethylene, propane, methanol, ethanol, acetaldehyde, methyl acetate, and ethyl acetate). The mol% of each product in the gas feed was used to calculate the selectivity ðSiÞ for each product using the following Eq. (1):

$$S_i = \frac{M_i \times n_i}{\sum_i M_i \times n_i} \times 100\% \quad (1)$$

where M_i is the mol% of product i detected and n_i is the number of carbons in product i. This definition of selectivity follows the work of Haider et al. who performed reactivity studies on similar catalyst systems [4]. As a measure of the overall activity, CO conversion (%) was also calculated for each catalyst via Eq. (2) as follows:

$$\text{CO conversion} = \frac{\sum_i M_i \times n_i}{M_{CO}} \times 100\% \quad (2)$$

where M_{CO} is the mol% of CO detected in the gas feed.

Prior to reaction, the sample was reduced at 300 oC under 9 mL/min H_2 flow at a pressure of 1 bar for 30 min (GHSV = 0.028 mL min^{-1} mm^{-3}). After reduction, the sample was cooled to room temperature in 9 mL/min H_2 flow, and the gas switched to a 4 mL/min H_2 flow + 2 mL/min CO flow at a pressure of 1 bar (GHSV = 0.019 mL min^{-1} mm^{-3}). The sample temperature was then raised to 240 oC to simulate CO hydrogenation reaction conditions; this temperature was chosen after performing the reaction at a range of temperatures and determining the best activity/selectivity for oxygenate production.

2.3. In situ structure determinations

The structures of the Fe–Rh/TiO_2 catalysts under different conditions were investigated by XRD and PDF at the X7B beamline at the National Synchrotron Light Source (NSLS) operating at a wavelength of 0.3196 Å. The powder diffraction pattern was collected with a Perkin Elmer amorphous silicon 2-D detector. The detector distance was changed from 400 mm for XRD to 180 mm for PDF measurements. The detector position was calibrated by measuring the diffraction from a sodium hexaboride standard at both detector positions. The sample was loaded into a 1.2-mm OD quartz capillary tube and plugged with quartz wool, then loaded into the same reactor cell as used for reactivity studies. Sample heating is achieved via two filament heaters located directly above and below the capillary to eliminate diffraction of the filaments. XRD and PDF data were collected on the as-synthesized samples and after reduction at 300 oC for 30 min under 9 mL/min H_2 flow at a pressure of 2 bar (GHSV = 0.191 mL min^{-1} mm^{-3}). After cooling to room temperature, XRD and PDF measurements were made on the reduced catalysts and then under CO hydrogenation conditions of 4 mL/min H_2 + 2 mL/min CO flow at 240 oC at a total pressure of 2 bar (GHSV = 0.127 mL min^{-1} mm^{-3}). XRD and PDF data were also collected for the bare support under identical conditions to compare with loaded catalysts for analysis by difference PDF (dPDF) where only the contributions of Fe and Rh are observed.

The XRD and PDF 2-D diffraction images were integrated into 1-D ''2h scans'' using the Fit2D software [17]. The Rietveld refinement of XRD data was performed with the EXPGUI-GSAS software package [18,19]. The analysis was completed by fitting the sample diffraction to an appropriate model where the lattice constants, scale factor, peak profile functions, and atomic potentials were varied to produce a simulated diffraction pattern nearly identical to the experimental XRD data. The models were chosen based upon knowledge of synthesis, reaction conditions, and phases previously identified in similar studies, that is, Rh metal, Fe metal, Fe-Rh alloys (FeRh and Fe0.7Rh0.3), FeO, Fe_2O_3, Fe_3C, Fe_2C, Fe_5C_2, anatase TiO_2, and rutile TiO_2 [20–32]. A complete refinement provides information about phase quantification, lattice constants, and particle size.

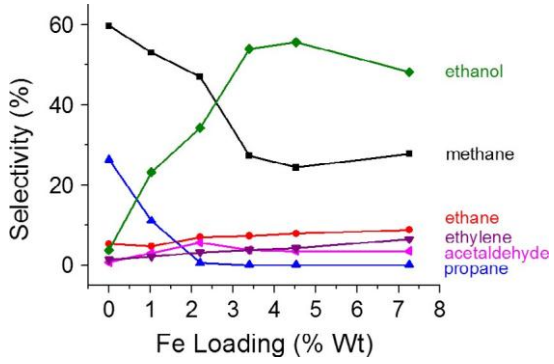

Fig. 1. Selectivity for various reaction products from CO hydrogenation versus Fe loading for """2 wt% Rh/TiO_2 catalyst samples. Reaction conditions: 2:1 H_2:CO gas mix at 1 bar total pressure and an operating temperature of 240 oC.

The PDF data were processed with the software package pdfgetX3 that provides a Fourier transform of the scattering function obtained from the diffraction pattern [33]. Ordinarily, PDF can be fitted against a model to quantifiably determine the particle size, coordination number, and order. In the catalysts studied here, the Fe and Rh components of interest are less than 10 wt% of the major phase, that is, the TiO_2 support, which makes the fit to the PDF data insensitive to structural parameters involving the Fe and Rh components. The difference PDF (dPDF), in which the scattering signal from the bare TiO_2 support is subtracted from that of the metal-loaded catalyst under the same conditions, allows the contributions from the minor phases to be observed more clearly; however, dPDF data include changes in support structure associated with the deposition of Fe and Rh which cannot be readily accounted for in structural models. Here, the dPDF data are used to qualitatively analyze the first shell atomic distances and coordination of the Fe and Rh components utilizing the phase information obtained from the XRD refinement and the phases identified in previous studies [4,8,9,15].

3. Results and discussion

3.1. Catalyst selectivity: product analysis by gas chromatography

The selectivities for various oxygenate products from CO hydrogenation over Fe-Rh/TiO_2 catalysts as a function of Fe content are shown in Fig. 1 and summarized in Table 2. These data were taken with 2:1 H_2:CO mix at a total pressure of 1 bar and a temperature of 240 oC. The results show that the initial loading of Fe increases the selectivity toward ethanol by a factor of six, while for the most prominent hydrocarbons (methane, propane) the selectivities are greatly reduced. The maximum ethanol selectivity (""55%) occurs at a loading of ""4.5 wt% Fe, whereas methane is less than half its initial value for the pure Rh catalyst. The decrease in selectivity for ethanol at even higher Fe loading (7 wt%) is accompanied by a slight increase in the hydrocarbon products.

The conversion of CO, as defined by Eq. (2), is shown in Fig. 2 as a function of Fe content. The results show that CO conversion drops significantly with the addition of Fe to the catalysts, which according to Fig. 1 is also associated with higher ethanol and lower methane selectivity. Under the reaction conditions used here, the Rh-only catalyst exhibits far greater CO conversion than the Fe-only catalyst (Table 2), although both produce mostly hydrocarbon products. The fact that mixing the two metals results in a significant shift in product distributions and a large drop in CO conversion indicates that the Fe and Rh components do not act independently, that is, segregated particles, but their admixture leads to reactive sites that are modified relative to the single-metal catalysts.

In general, the observed trends in methane and oxygenate selectivity versus Fe loading are consistent with those found in previous studies of CO hydrogenation on similar bimetallic Fe-/Rh-supported catalysts [4,6]. Burch and Hayes found that the

Table 2
Conversion and selectivity for various products (%) from the CO hydrogenation reaction on the Fe-modified Rh/TiO_2 catalyst samples (listed in Table 1). Selectivity calculations based on Eq. (1) in the text. Conversion calculated from Eq. (2) in the text.

Sample	Methane (%)	Ethane (%)	Ethylene (%)	Propane (%)	Methanol (%)	Ethanol (%)	Acetaldehyde (%)	Conversion (%)
Rh	59.7	5.2	1.3	26.3	0.4	3.7	0.7	11.18
Fe	–	100	–	–	–	–	–	0.03
1FeRh	53.1	4.8	2.1	11.0	1.3	23.1	2.9	4.34
2FeRh	47.0	7.0	3.1	0.3	1.7	34.2	5.5	2.80
3FeRh	27.2	7.2	3.8	–	4.0	54.0	3.8	1.52
4FeRh	24.3	7.9	4.2	–	4.4	55.6	3.5	1.25
7FeRh	27.8	8.8	6.5	–	4.8	48.1	3.5	1.59

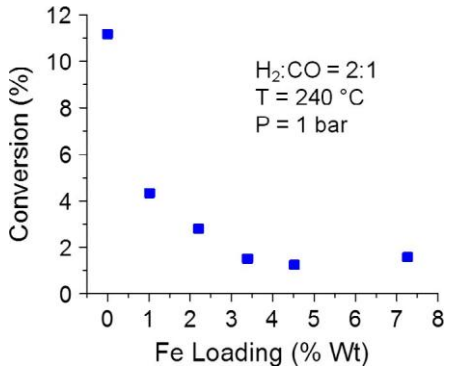

Fig. 2. Total conversion of CO versus Fe loading for """2 wt% Rh/TiO_2 catalyst samples. Reaction conditions: 2:1 H_2:CO gas mix at 1 bar total pressure and an operating temperature of 240 oC.

ethanol selectivity increases up to 10 wt% Fe loading for Rh-/Al_2O_3-supported catalysts with a small but concurrent increase in CO conversion using a reaction pressure of 10 bar and a 1:1 feed of H_2:CO [6]. More recently, Haider, et al. reported that changing the support from SiO_2 to TiO_2 dramatically increases oxy- genate selectivity with a maximum (""37%) occurring for Fe load- ings of 5 wt% [4]. Moreover, they found that CO conversion at a reaction pressure of 20 bar (1:1 H_2:CO) decreased for titania-supported catalysts with Fe loadings higher than 2.5 wt%. Our results in Figs. 1 and 2 are generally in agreement with previ- ous studies using titania as a support, where Fe addition leads to enhanced ethanol selectivity and the suppression of methane. However, Fe addition does not enhance CO conversion at any of the concentrations reported here. Instead, the addition of Fe signif-icantly lowers the overall activity of the catalysts, with the largest percentage drop occurring at the smallest Fe loadings tested. A possible cause for the differences in conversion versus Fe addition obtained in this work may be due to the lower reaction pressure (1 bar) compared with that used in previous studies (10–20 bar) [4,6].

3.2. Catalyst morphology: ex situ TEM

The morphology and atomic composition of the Fe–Rh/TiO_2 cat-alyst particles used in the above reactivity studies were character-ized by HRTEM and EDS, respectively. Fig. 3 shows the combined microscopy results for a reduced Fe–Rh catalyst (2FeRh), which exhibits enhanced activity for ethanol synthesis (see Fig. 1). The particles show an average particle diameter of 1.8 ± 0.2 nm, but more importantly, Rh and Fe were always found together in single-particle scans with EDS, indicating close contact between Rh and Fe. Moreover, lattice fringe analyses show crystalline parti-cles with a lattice spacing of 2.11 Å. This spacing is consistent with the (1 1 0) plane of FeRh with a space group of pm-3m [20,21]. Given that HRTEM is heavily dependent on crystal orientation, not observing lattice fringes due to metallic Rh, does not rule out the possibility of its existence. The only changes that are evident in the postreaction catalyst are a slight sintering of the particles to a diameter of 2.0 ± 0.2 nm and a small amount of carbon depo-sition (images and EDS of postreaction catalysts are shown in SI, Figs. S1–S3). The minor increase in particle diameter and narrow size distribution observed in the postreaction catalysts indicate that these particles are robust and relatively resistant to sintering under reaction conditions. Fig. 4 shows HRTEM, EDS, and the size distribution of the 7FeRh catalyst, where the particles with a larger Fe loading are found to have a similar average particle diameter of 1.9 ± 0.2 nm and EDS gives an Fe:Rh ratio approximately 4–5 times higher. Observed lattice fringes decrease to 2.08 Å, which is consis-tent with an increase in Fe concentration of the alloy. The changes that occur in 7FeRh during the reaction are similar to 2FeRh, a slight sintering of the particles and carbon deposition, which is shown in the SI (Figs. S1–S3).

The EDS and lattice fringe analyses provide evidence for the presence of FeRh alloy particles, or at least a surface Fe-Rh alloy on Rh metal nanoparticles, in both the reduced and postreaction catalysts. FeO_x is likely to be present due to Fe's high oxidation potential, and the detection of carbon in the postreaction samples may also indicate the presence of Fe carbides. We attribute the lack of visualizing the Fe oxides and/or carbides to the high dispersion of the phases and poor contrast from the titania support, which greatly reduces their visibility in TEM. A more detailed structural and phase analysis of the Fe–Rh/TiO_2 catalysts under reaction con-ditions is presented below.

3.3. Catalyst structure under reaction conditions: in situ XRD and dPDF

Reactivity studies discussed above confirm that Fe addition enhances selectivity toward ethanol and suppresses methane selectivity. Previous structural studies concluded that the Fe mod-ification is due to intimate contact between Fe, Rh, and TiO_2, but the nature of interaction of Rh and Fe is still unclear [5,15]. In order to better understand the Fe and Rh phases in the catalysts, we focus mostly on the regions of the XRD patterns associated with Fe metal diffraction shown in Fig. 5 (the full XRD patterns of the catalysts are given in SI, Figs. S4 and S5). The assignments of the diffraction features are based on quantitative results obtained from Rietveld refinements of the XRD data. All known alloy structures of

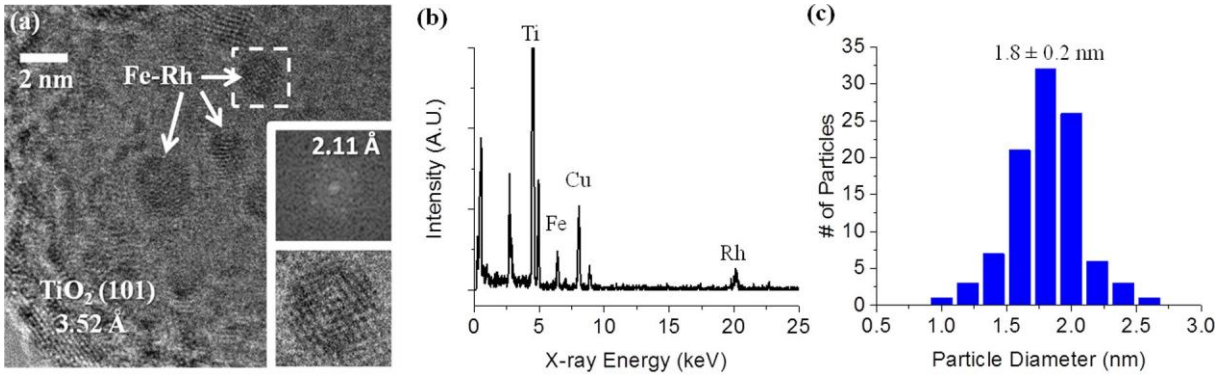

Fig. 3. Transmission electron microscopy results for the 2FeRh catalyst sample (see Table 1) following reduction: (a) HRTEM of Fe–Rh nanoparticles with FT of image and lattice fringe spacing assignment. (b) Single-particle EDS of Fe–Rh/Rh nanoparticle showing Fe and Rh together. (c) Size distribution of particle diameter.

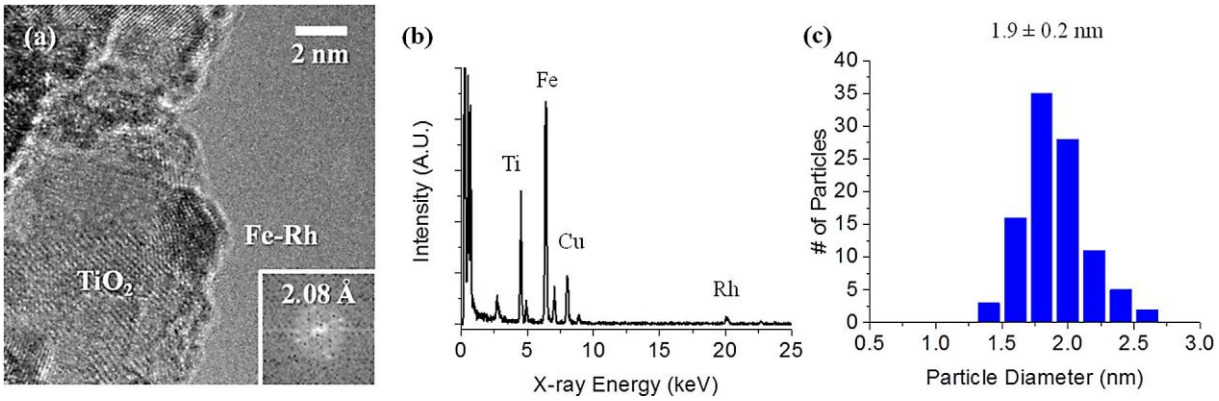

Fig. 4. Transmission electron microscopy results for the 7FeRh catalyst sample (see Table 1) following reduction: (a) HRTEM of Fe–Rh nanoparticles with FT of image and lattice fringe spacing assignment. (b) Single-particle EDS of Fe–Rh/Rh nanoparticle showing Fe and Rh together. (c) Size distribution of particle diameter.

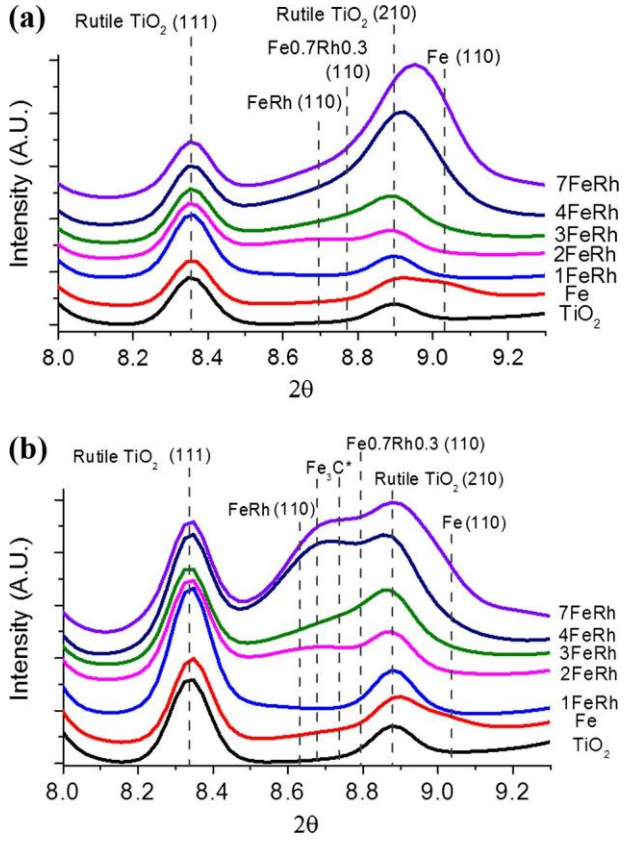

Fig. 5. Powder X-ray diffraction (XRD) curves for various Fe-modified Rh/TiO_2 catalysts (see Table 1 for definition of labels) for different treatment conditions: (a) after reduction in H_2 at 300 oC; (b) during CO hydrogenation reaction conditions using a 2:1 H_2:CO gas mix at 1 bar total pressure, and an operating temperature of 240 oC. (1 1 0) reflection for Fe_3C is at 8.68o (2h), and (0 0 2) reflection for Fe_3C is at 8.73o (2h).

Rh and Fe were considered, and refinement was attempted on each, but only FeRh and Fe0.7Rh0.3 were plausible based on peak positions and intensity ratios [20,21]. For the catalysts under CO hydrogenation, the presence of Fe oxide and carbide phases was also included in the refinement.

Fig. 5a shows XRD for the reduced catalysts in the range where diffraction features from Fe and Fe-Rh alloying are expected to appear. The Rh-only sample is not included, because the diffraction peaks due to metallic or oxidized Rh are overlapped by diffraction from the TiO_2 support. The Fe-only sample exhibits a broad shoulder centered at 9o (2h) which is attributable to the (1 1 0) reflection of metallic Fe [22]. The Fe-Rh bimetallic catalysts show a different shoulder which starts at 8.67o and shifts to slightly higher 2h with increasing Fe content. This new feature is due to the alloying of Rh and Fe, and the shift to higher 2h is from the formation of more Fe-rich alloys, as would be expected from the change in Fe:Rh ratio [20,21]. The refinement data for the reduced catalysts (Table 3) show that the introduction of Fe results in the formation of FeRh, which is accompanied by Fe0.7Rh0.3 at higher Fe loading. The latter is not unexpected, but the Fe content in the alloy is clearly limited as can be seen by the appearance of metallic Fe at the highest loadings (4FeRh, 7FeRh), where lower loadings only show metallic Fe alloyed with Rh.

The XRD patterns for catalysts under CO hydrogenation reaction conditions are shown in Fig. 5b. For the (1–3) FeRh catalysts, the composition is seen to be unchanged from their reduced state prior to reaction. The XRD patterns for catalysts at higher Fe content (4FeRh, 7FeRh) show a shift in scattering intensity from higher to lower 2h with a definitive shoulder appearing at 8.7o. At first glance, this shift appears to be from the increase in the Fe-Rh alloy. However, this shift can also be accounted for by the introduction of a carbide phase into the Rietveld refinement. Multiple iron carbides were considered (Fe_5C_2, Fe_2C, and Fe_3C), but the refinement resulted in the addition of only the Fe_3C phase. According to the refinement results summarized in Table 3, the Fe metal content is reduced at the expense of Fe_3C formation. Carburization of Fe is not unexpected as the reaction conditions for CO hydrogenation are very similar to Fischer–Tropsch synthesis (FTS) where Fe carbides are formed regardless of the initial phase of the catalyst [27,29,30]. Fe_3C is generally accepted as a spectator or deactivation phase, and therefore, its contribution in the CO conversion and product distribution is not expected to be substantial [30,34,35].

The Fe phase composition of the Fe–Rh catalysts obtained by Rietveld refinement of the XRD data is shown in Fig. 6 following

Table 3
Quantification of the Fe phase composition (wt%) derived from Rietveld refinements of the XRD data for the Fe-modified Rh/TiO_2 catalysts (listed in Table 1) after reduction in H_2 and under CO hydrogenation reaction conditions. Errors from the Rietveld refinements are shown in parentheses.

Sample	Fe/metal reduced	Fe/metal reaction	Fe/alloy reduced	Fe/alloy reaction	Fe/Fe_3C reaction
1FeRh	–	–	0.5 (2)	0.5 (2)	–
2FeRh	–	–	0.75 (9)	0.65 (9)	–
3FeRh	–	–	1.1 (3)	1.0 (4)	–
4FeRh	1.5 (3)	–	1.3 (3)	1.3 (4)	0.9 (2)
7FeRh	3.0 (4)	1.6 (3)	1.0 (3)	1.0 (4)	0.9 (2)

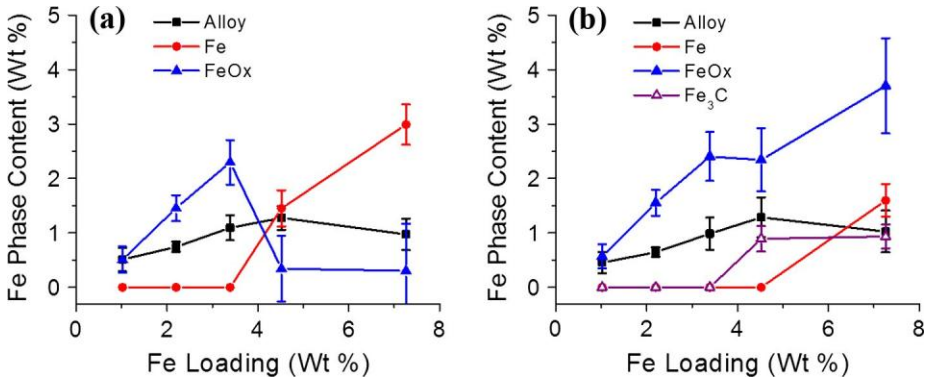

Fig. 6. A comparison of the amount of different Fe phases versus the total Fe loading for """2 wt% Rh/TiO_2 catalyst samples after (a) H_2 reduction and (b) under CO hydrogenation reaction conditions.

H_2 reduction and under reaction conditions. For the reduced catalysts (Fig. 6a), the amount of Fe incorporated into Fe–Rh alloys increases to a maximum near """4.5 wt% Fe, beyond which the alloyed fraction of Fe decreases. Moreover, the metallic Fe content in the reduced samples increases sharply at higher Fe loadings suggesting that Fe metal segregation occurs which limits the amount of Fe that is incorporated into the Fe–Rh alloy. Under reaction conditions (Fig. 6b), the amount of Fe–Rh alloy is essentially unchanged, whereas part of the metallic Fe content is apparently transformed to the Fe_3C carbide phase. Overall, the Fe content accounted for by metallic Fe, Fe–Rh alloy, and Fe_3C phases is still less than that determined by elemental analysis. The unaccounted for Fe content could be present as a FeO_x phase which is not observed via XRD for a similar reason as with TEM, that is, high dispersion and low crystallinity [36,37].

Assuming all the unaccounted for Fe is present as an oxide, estimates of the FeO_x content were obtained by subtracting the total Fe content obtained by XRD refinement (metallic, alloy, carbide) from the total Fe loading obtained from ICP analyses. The FeO_x content obtained in this way for each catalyst is included in Fig. 6. For the reduced catalysts (Fig. 6a), the FeO_x content may be overestimated at low Fe loadings (<3 wt%) due to difficulties in isolating the metallic Fe phase in the XRD refinements for those samples, but at higher Fe content, the oxide is apparently converted to Fe metal by hydrogen reduction. By comparison, FeO_x is the major Fe phase for all catalysts under CO hydrogenation conditions (Fig. 6b). The sharp rise in FeO_x at the highest Fe loading (7 wt%) is likely due to oxidation of the relatively large fraction of metallic Fe in the reduced 7FeRh sample prior to reaction (Fig. 6a). Hence, both the Fe oxide and carbide phase contents under reaction conditions appear to be primarily a result of transformation of metallic Fe in the catalysts prior to reaction.

While XRD identifies the phase composition and long-range ordering of the catalysts, it provides little information about the local atomic structure of the active phases in the catalysts. PDF has the benefit of resolving the local structure, and the further implementation of dPDF allows us to examine only the supported metals deposited which are believed to be the active components of the catalysts. The dPDF of the reduced catalysts is shown in Fig. 7a. Based on previous studies, the first shell peak at 2.76 Å in the Rh-only data can be assigned to the Rh–Rh bond [14,38–40]. With the addition of Fe, this peak begins to broaden and eventually splits into two distinct peaks at 2.53 Å and 2.79 Å at the highest Fe loading. The 2.53 Å distance is indicative of a Fe–Rh or Fe–Fe bond, whereas the peak at 2.79 Å can be attributed to Rh–Rh in the FeRh alloy or a second nearest neighbor of Fe in metallic Fe [41]. The appearance of these two features at higher Fe loading confirms that Fe is being incorporated into a Fe–Rh alloy, and in the case of Fe loading >3 wt%, also forming metallic Fe. A peak due to Fe–O can be observed at """2 Å, but a distinct modulation in intensity or distance is not observed. However, it is clear that only Fe-containing catalysts exhibit a significant peak consistent with a metal–oxygen bond distance. The increase in the area of the peaks associated with metal–metal bonding (2.5–2.9 Å) also signifies that the coordination of Rh and Fe is growing as well. From the Rietveld refinement results in Table 1, changes in coordination can be associated with the growth of both Fe–Rh and Fe–Fe domains. Overall, these observations are consistent with the XRD data, which also show the Fe–

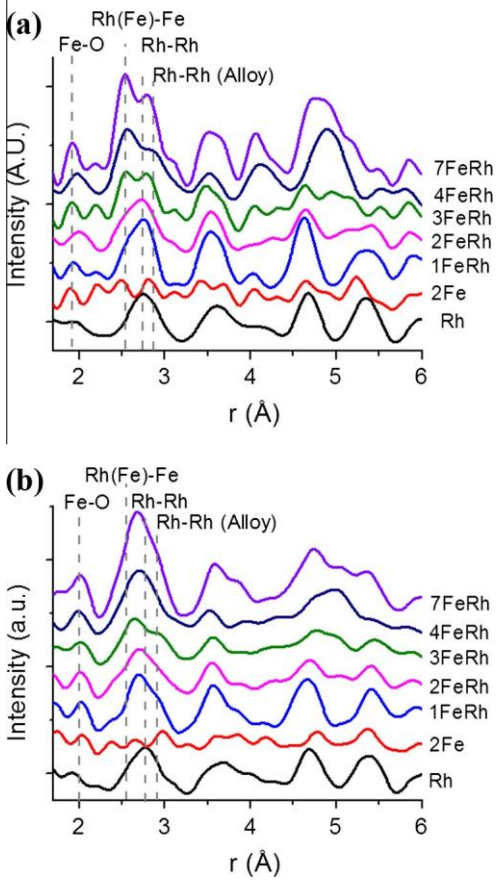

Fig. 7. Differential pair distribution functions (dPDF) after removal of the TiO_2 contributions for different Fe-Rh/TiO_2 catalysts (see Table 1 for definition of labels) for different treatment conditions: (a) after reduction in H_2 at 300 oC; (b) during CO hydrogenation reaction conditions using a 2:1 H_2:CO gas mix at 1 bar total pressure and an operating temperature of 240 oC.

Rh/Fe–Fe contribution increasing with higher Fe loading. One notable difference between the dPDF and XRD data is the observation of metallic Rh–Rh bonds suggesting isolated domains of metallic Rh. The latter could be explained by core–shell particles with Fe–Rh alloys in the near surface region and internal cores of metallic Rh. This is consistent with the theoretical work by Yang and Liu where Fe was expected to segregate to the surface of Rh and the EXAFS study of Ichikawa and Fukishima where the majority of Fe exists in the oxide phase at the interface between Rh and the support, while Fe^0 exist on the surface of the Rh nanoparticles [7,15].

Fig. 7b shows the dPDF curves for the same catalysts under CO hydrogenation conditions (240 oC, 2:1 H_2:CO ratio @ 6 mL/min). The most apparent change compared to the reduced catalysts is that the first shell peak has shifted closer to Rh–Rh bond distances and has increased in width, indicative of a decrease in the Fe–Rh and Fe–Fe coordination with respect to Rh–Rh. At the highest Fe loadings, the first shell peak is broad and centered at an intermediate metal–metal bond distance of 2.66 Å. This suggests multiple components with a range of Rh–Rh and Fe–Rh distances and coordination environments. From the XRD results, we know that Fe metal formed during the reduction at high Fe loadings (>4 wt%) is lost to carburization and oxidation. This would lead to a loss of coordination in the Fe–Fe peak and a decrease in the intensity of the peak at 2.53 Å. Hence, the first shell peak is mostly representative of Rh–Rh coordination. Overall, the changes in the peak intensities and positions are consistent with the trends observed in XRD. Again, there is no noticeable change in the feature attributed to Fe–O, but the dPDF data suggest that FeO_x is present for all Fe loadings.

As described above and shown in Figs. 6 and 7, the compositions of the Fe and Rh metal phases change significantly with Fe loading and under reaction conditions. To see how this correlates with selectivity of the catalysts, the selectivity data for ethanol and methane formation are plotted in Fig. 8 along with the Fe alloy, metal, carbide, and oxide phase compositions for all the catalysts studied. As seen in Fig. 8a, the ethanol selectivity closely correlates with the FeRh alloy content, but not the Fe_3C carbide phase which is only seen at the highest Fe loadings studied (4FeRh and 7FeRh). The FeO_x content also follows ethanol selectivity except at higher Fe loading where the selectivity decreases but the oxide content continues to increase. The latter is most likely due to the increase in metallic Fe content in the reduced catalysts at higher Fe loading (4FeRh and 7FeRh) which is oxidized to FeO_x under reaction conditions. The concomitant decrease in methane selectivity also correlates with Fe-Rh alloy and Fe oxide phase content as shown in Fig. 8b. These comparisons suggest that the presence of Fe-Rh alloys enhances ethanol selectivity and simultaneously suppresses methane, whereas Fe_3C formation does not appear to have a significant effect on product distribution. This is consistent with the role of Fe_3C in FTS which is thought to be a spectator or deactivator phase [30,34,35]. The importance of FeO_x in influencing selectivity is less clear, but its presence under reaction conditions (Fig. 7b) suggests that it is acting synergistically with the Fe–Rh alloy (or pure Rh), as the Fe-only sample shows essentially no ethanol formation under these reaction conditions. The interface with FeO_x could influence product selectivity by modifying or blocking sites on the Rh active phase and more generally acting to enhance selectivity similar to changing the Rh support from SiO_2 to TiO_2.

Overall, these data support the general conclusion that Fe–Rh alloys enhance ethanol selectivity, while simultaneously suppressing methane. Due to the intimate Fe–Rh contact in the alloy fractions, the Fe is likely altering both the number and nature of active Rh sites, which allows ethanol synthesis to compete with methane formation. Density functional theory (DFT) calculations and kinetic Monte Carlo (KMC) simulations suggest that the key factors determining the selectivity of Fe-doped Rh surfaces for ethanol formation are the relative barriers for methyl hydrogenation,

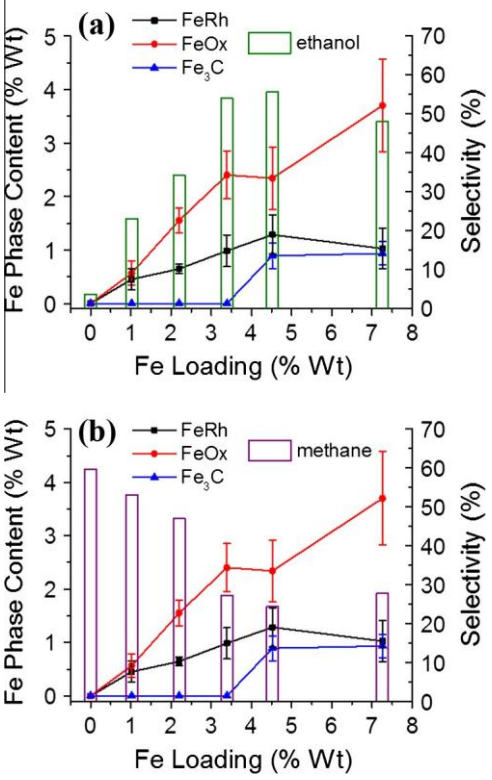

Fig. 8. Comparisons of product selectivity for CO hydrogenation with the Fe phase content of Fe-Rh/TiO_2 catalysts as a function of Fe loading; (a) selectivity for total oxygenates and ethanol production and Fe content in alloy and oxide phases; (b) selectivity for methane production and Fe content in alloy and oxide phases. Reaction conditions: 2:1 H_2:CO gas mix at 1 bar total pressure and an operating temperature of 240 oC.

$CH_{3(a)} + H_{(a)} \rightleftharpoons CH_{4(g)}$, and CO insertion, $CH_{3(a)} + CO_{(a)} \rightleftharpoons CH_3CO_{(g)}$ [7,12]. The latter reaction leads to ethanol after subsequent hydrogenation steps. According to the calculations, Fe addition lowers the barrier to the CO insertion step and thereby increases selectivity of ethanol relative to methane [7]. Our conclusion that a surface Fe–Rh alloy contributes to the improved ethanol selectivity is consistent with the main findings of these calculations, which were based on Fe-doped Rh surfaces with both metals participating. This also explains the slight decrease in ethanol selectivity at the highest Fe loading where phases other than the Fe–Rh alloy (Fe metal, FeO_x, and Fe_3C) become more prevalent.

4. Summary

The combined results from TEM, XRD, and dPDF provide clear evidence for the presence of FeRh alloy in mixed Fe and Rh catalysts following reduction and during CO hydrogenation. Specifically, the presence of Fe–Rh alloy observed in TEM is supported by the Rietveld refinements of the XRD data and trends in the dPDF data, all of which show that the alloy concentration increases with increasing Fe content. Furthermore, the XRD results indicate that a substantial fraction of metallic Fe is both carburized and oxidized during CO hydrogenation. The dPDF data also point to the presence of a pure Rh phase, which becomes more pronounced during CO hydrogenation conditions. The latter may suggest that Fe and Rh form a surface alloy, with the core of the particle being pure Rh.

The overall picture to emerge is that at low Fe loadings, the Fe is partially incorporated into the Rh nanoparticles as a surface Fe–Rh alloy. The remaining amount of Fe is tied up in oxide formation

which could be located near the Rh nanoparticles or on the TiO_2 support. The amount of surface alloy increases with increasing Fe loading up to ""4 wt%, beyond which segregation to metallic Fe becomes favored over Fe–Rh alloy formation. During CO hydrogenation conditions, the metallic Fe deposits and some of the Fe in the surface alloy are converted to both oxide and carbide phases. Although Fe_3C is present on high Fe-loading catalysts (4FeRh and 7FeRh), no substantial correlation is found with conversion or product distribution. This could be related to the fact that Fe_3C is suspected as a spectator/deactivator phase in FTS.

The combined correlation (Fig. 8) of Fe–Rh alloy and FeO_x content with increases in ethanol selectivity and methane suppression suggests that FeO_x may also play a role in ethanol synthesis. The fact that the CO conversion is a minimum for the highest ethanol selectivity and lowest methane selectivity (Figs. 1 and 2) also suggests that the enhancement role of Fe–Rh alloy and FeO_x is the modification and/or blocking of Rh sites responsible for methane and/or other side reactions. These findings are consistent with the conclusions of early studies that the interface between Rh and Fe is responsible for suppression of catalytic activity due to the blocking of active sites [5,6].

Acknowledgments

This work was supported by the U.S. Department of Energy, Office of Science, Office of Basic Energy Sciences under Contract No. DE-SC0012704. The XRD and PDF data were taken at the National Synchrotron Light Source, which is a DOE Office of Science User Facility located at Brookhaven National Laboratory. R.P. and M.G.W. would like to acknowledge Charles T. Black at the Center for Functional Nanomaterials at Brookhaven National Laboratory for helpful discussions and assistance in catalysts' syntheses. J.L. is Serra Húnter Fellow and is grateful to ICREA Academia program.

References

[1] G.C. Chinchen, P.J. Denny, J.R. Jennings, M.S. Spencer, K.C. Waugh, Synthesis of methanol: part 1. Catalysts and kinetics, Appl. Catal. 36 (1988) 1–65.
[2] J.J. Spivey, A. Egbebi, Heterogeneous catalytic synthesis of ethanol from biomass-derived syngas, Chem. Soc. Rev. 36 (2007) 1514–1528.
[3] V. Subramani, S.K. Gangwal, A review of recent literature to search for an efficient catalytic process for the conversion of syngas to ethanol, Energy Fuels 22 (2008) 814–839.
[4] M.A. Haider, M.R. Gogate, R.J. Davis, Fe-promotion of supported Rh catalysts for direct conversion of syngas to ethanol, J. Catal. 261 (2009) 9–16.
[5] M.R. Gogate, R.J. Davis, X-ray absorption spectroscopy of an Fe-promoted Rh/TiO_2 catalyst for synthesis of ethanol from synthesis gas, ChemCatChem 1 (2009) 295–303.
[6] R. Burch, M.J. Hayes, The preparation and characterisation of Fe-promoted Al_2O_3-supported Rh catalysts for the selective production of ethanol from syngas, J. Catal. 165 (1997) 249–261.
[7] L. Yang, P. Liu, Ethanol synthesis from syngas on transition metal-doped Rh(1 1 1) surfaces: a density functional kinetic Monte Carlo study, Top. Catal. 57 (2014) 125–134.
[8] S. Sakellson, M. McMillan, G.L. Haller, EXAFS evidence for direct metal-metal bonding in reduced rhodium/titania catalysts, J. Phys. Chem. 90 (1986) 1733–1736.
[9] D.E. Resasco, R.S. Weber, S. Sakellson, M. McMillan, G.L. Haller, X-ray absorption near-edge structure evidence for direct metal–metal bonding and electron transfer in reduced rhodium/titania catalysts, J. Phys. Chem. 92 (1988) 189–193.
[10] J.H.A. Martens, R. Prins, H. Zandbergen, D.C. Koningsberger, Structure of rhodium/titania in the normal and the SMSI state as determined by extended X-ray absorption fine structure and high-resolution transmission electron microscopy, J. Phys. Chem. 92 (1988) 1903–1916.
[11] E. Guglielminotti, F. Pinna, M. Rigoni, G. Strukul, L. Zanderighi, The effect of iron on the activity and the selectivity of Rh/ZrO_2 catalysts in the CO hydrogenation, J. Mol. Catal. A: Chem. 103 (1995) 105–116.
[12] Y. Choi, P. Liu, Mechanism of ethanol synthesis from syngas on Rh(1 1 1), J. Am. Chem. Soc. 131 (2009) 13054–13061.
[13] J.R. Katzer, A.W. Sleight, P. Gajardo, J.B. Michel, E.F. Gleason, S. McMillan, The role of the support in CO hydrogenation selectivity of supported rhodium, Faraday Discuss. 72 (1981) 121–133.
[14] P. Johnston, R.W. Joyner, P.D.A. Pudney, The interaction of synthesis gas (CO–H,) with small rhodium particles, J. Phys.: Condens. Matter 1 (1989) SB171–SB176.
[15] M. Ichikawa, T. Fukushima, T. Yokoyama, N. Kosugi, H. Kuroda, EXAFS evidence for direct rhodium–iron bonding in silica-supported rhodium–iron bimetallic catalysts, J. Phys. Chem. 90 (1986) 1222–1224.
[16] P.J. Chupas, K.W. Chapman, C. Kurtz, J.C. Hanson, P.L. Lee, C.P. Grey, A versatile sample-environment cell for non-ambient X-ray scattering experiments, J. Appl. Crystallogr. 41 (2008) 822–824.
[17] A.P. Hammersley, S.O. Svensson, M. Hanfland, A.N. Fitch, D. Hausermann, Two-dimensional detector software: from real detector to idealised image or two-theta scan, High Pressure Res. 14 (1996) 235–248.
[18] A.C. Larson, R.B. Von Dreele, General Structure Analysis System (GSAS), Los Alamos Laboratory Report LAUR 86-748, 2004.
[19] B. Toby, EXPGUI, a graphical user interface for GSAS, J. Appl. Crystallogr. 34 (2001) 210–213.
[20] Y. Ohtani, I. Hatakeyama, Antiferro-ferromagnetic transition and microstructural properties in a sputter deposited FeRh thin film system, J. Appl. Phys. 74 (1993) 3328–3332.
[21] A. Houben, P. Müller, J. von Appen, H. Lueken, R. Niewa, R. Dronskowski, Synthesis, crystal structure, and magnetic properties of the semihard itinerant ferromagnet $RhFe_3N$, Angew. Chem. Int. Ed. 44 (2005) 7212–7215.
[22] F.W. Von Batchelder, R.F. Raeuchle, Re-examination of the symmetries of iron and nickel by the powder method, Acta Crystallogr. 7 (1954) 464.
[23] B.T.M. Willis, H.P. Rooksby, Change of structure of ferrous oxide at low temperature, Acta Crystallogr. 6 (1953) 827–831.
[24] R.E.H.R.L. Blake, Tubor Zoltai, Larry W. Finger, Refinement of the hematite structure, Am. Mineral. 51 (1966) 7.
[25] M. Černohorský, The ratio method for absolute measurements of lattice parameters with cylindrical cameras, Acta Crystallogr. 13 (1960) 823–826.
[26] K.V.K. Rao, S.V.N. Naidu, L. Iyengar, Thermal expansion of rutile and anatase, J. Am. Ceram. Soc. 53 (1970) 124–126.
[27] K. Xu, B. Sun, J. Lin, W. Wen, Y. Pei, S. Yan, M. Qiao, X. Zhang, B. Zong, e-Iron carbide as a low-temperature Fischer–Tropsch synthesis catalyst, Nat. Commun. 5 (2014).
[28] D.H. Chun, J.C. Park, S.Y. Hong, J.T. Lim, C.S. Kim, H.-T. Lee, J.-I. Yang, S. Hong, H. Jung, Highly selective iron-based Fischer–Tropsch catalysts activated by CO_2-containing syngas, J. Catal. 317 (2014) 135–143.
[29] E. de Smit, F. Cinquini, A.M. Beale, O.V. Safonova, W. van Beek, P. Sautet, B.M. Weckhuysen, Stability and reactivity of e–v–h iron carbide catalyst phases in Fischer–Tropsch synthesis: controlling lC, J. Am. Chem. Soc. 132 (2010) 14928–14941.
[30] E. de Smit, A.M. Beale, S. Nikitenko, B.M. Weckhuysen, Local and long range order in promoted iron-based Fischer–Tropsch catalysts: a combined in situ X-ray absorption spectroscopy/wide angle X-ray scattering study, J. Catal. 262 (2009) 244–256.
[31] K. Sudsakorn, J.G. Goodwin Jr., A.A. Adeyiga, Effect of activation method on Fe FTS catalysts: investigation at the site level using SSITKA, J. Catal. 213 (2003) 204–210.
[32] D.B. Bukur, K. Okabe, M.P. Rosynek, C.P. Li, D.J. Wang, K.R.P.M. Rao, G.P. Huffman, Activation studies with a precipitated iron catalyst for Fischer–Tropsch synthesis: I. Characterization studies, J. Catal. 155 (1995) 353–365.
[33] P. Juhas, T. Davis, C.L. Farrow, S.J.L. Billinge, PDFgetX3: a rapid and highly automatable program for processing powder diffraction data into total scattering pair distribution functions, J. Appl. Crystallogr. 46 (2013) 560–566.
[34] J.F. Bengoa, A.M. Alvarez, M.V. Cagnoli, N.G. Gallegos, S.G. Marchetti, Influence of intermediate iron reduced species in Fischer–Tropsch synthesis using Fe/C catalysts, Appl. Catal. A 325 (2007) 68–75.
[35] T. Herranz, S. Rojas, F.J. Pérez-Alonso, M. Ojeda, P. Terreros, J.L.G. Fierro, Genesis of iron carbides and their role in the synthesis of hydrocarbons from synthesis gas, J. Catal. 243 (2006) 199–211.
[36] K.-I. Shimizu, A. Satsuma, T. Hattori, Selective catalytic reduction of NO by hydrocarbons on Ga_2O_3/Al_2O_3 catalysts, Appl. Catal. B 16 (1998) 319–326.
[37] Y.-Y. Huang, B.-Y. Zhao, Y.-C. Xie, A novel way to prepare silica supported sulfated titania, Appl. Catal. A 171 (1998) 65–73.
[38] K. Teramura, S.-I. Okuoka, S. Yamazoe, K. Kato, T. Shishido, T. Tanaka, In situ time-resolved energy-dispersive XAFS study on photodeposition of Rh particles on a TiO_2 photocatalyst, J. Phys. Chem. C 112 (2008) 8495–8498.
[39] H. Kuroda, T. Yokoyama, K. Asakura, Y. Iwasawa, Temperature-dependence of EXAFS spectra of supported small metal particles, Faraday Discuss. 92 (1991) 189–198.
[40] P. Johnston, R.W. Joyner, P.D.A. Pudney, E.S. Shpiro, B.P. Williams, In situ studies of supported rhodium catalysts, Faraday Discuss. 89 (1990) 91–105.
[41] H. Tanaka, R. Kaino, K. Okumura, T. Kizuka, Y. Nakagawa, K. Tomishige, Comparative study of Rh/MgO modified with Fe, Co or Ni for the catalytic partial oxidation of methane at short contact time. Part I: characterization of catalysts, Appl. Catal. A 378 (2010) 175–186.